RESEARCH ARTICLE

The stable atmospheric boundary layer over snow-covered sea ice: Model evaluation with fine-scale ISOBAR18 observations

T. Lorenz[1] ⬤ | S. Mayer[1] | S. T. Kral[2] | I. Suomi[3] ⬤ | G.-J. Steeneveld[4] ⬤ |
A. A. M. Holtslag[4]

[1]NORCE Norwegian Research Centre,
Bjerknes Centre for Climate Research,
Bergen, Norway

[2]Geophysical Institute and Bjerknes
Centre for Climate Research, University of
Bergen, Bergen, Norway

[3]Finnish Meteorological Institute,
Helsinki, Finland

[4]Meteorology and Air Quality Section,
Wageningen University, Wageningen, The
Netherlands

Correspondence
T. Lorenz, NORCE Norwegian Research
Centre, Bjerknes Centre for Climate
Research, Bergen, Norway.
Email: torge.lorenz@norceresearch.no

Abstract

A realistic representation of the stable atmospheric boundary layer in numerical weather prediction (NWP) and climate models is still a challenge. We study the evolution of a stable boundary layer over snow-covered sea ice in Bothnian Bay during wintertime in 2018. We perform high-resolution model experiments with the Weather Research and Forecasting model in its single-column model configuration and its default mesoscale configuration to assess which physical processes are essential to predict near-surface variables correctly. We evaluate our model runs against the unique observational dataset collected during ISOBAR18, which combines novel, upper-air measurements by an uncrewed aircraft system with wind lidar, sodar, and conventional meteorological mast data. By analysing surface fluxes in the single-column model, we demonstrate how the atmospheric cooling at the ground can be modelled more realistically than in the mesoscale set-up. We show that surface albedo and sea-ice thickness are essential for the surface energy balance in the model, and we demonstrate how the surface fluxes in the mesoscale downscaling with default settings are subject to strong biases. We also show that the ERA5 reanalysis is not capable of representing the observed surface meteorology in the stable atmospheric boundary layer. Our study illustrates the importance of surface albedo and sea-ice thickness for NWP models. Though a seasonal snow albedo is already in use in many NWP settings, the routine inclusion of sea-ice thickness, in particular, would be a great step forward for weather forecasts and regional climate simulations.

KEYWORDS
ISOBAR, numerical weather prediction, sea ice, single-column model, stable boundary layer, UAS measurements

1 | INTRODUCTION

Shallow stable atmospheric boundary layers (SABLs) often develop over ice or snow-covered surfaces in calm and clear-sky conditions (Mahrt, 2014). Near-surface meteorology under such conditions still provides a challenge for numerical weather prediction (NWP) and climate models (e.g., Walsh *et al.*, 2008; Atlaskin and Vihma, 2012; Mayer *et al.*, 2012; Holtslag *et al.*, 2013; Davy and Esau, 2016; Hewson, 2019; Schneider *et al.*, 2022). This is mainly due to three reasons. First, the subgrid-mixing schemes in such models typically rely on Monin–Obukhov similarity theory (MOST; Monin and Obukhov, 1954) to represent turbulent mixing which is not directly resolved by the numerical grid. MOST, however, does not universally apply to turbulence properties in the SABL, especially under very stable conditions (Mahrt, 2014). This issue is tied in strongly with the second reason: a too coarse vertical resolution close to the ground. Each additional vertical level in NWP models comes with an immediate, proportional increase in computational costs, which effectively limits the number of vertical levels in operational weather forecasts and multidecadal climate simulations. As a result, steep gradients in meteorological variables close to the ground cannot be resolved properly, and physical processes in the SABL are not modelled correctly. Third, local surface conditions (like land use, vegetation, and soil type) may be either crudely approximated by the land-surface model or misrepresented by the coarse horizontal spacing in the numerical grid. The combination of these issues has severe implications on weather forecasts and climate projections whenever stable stratification prevails, and especially in the polar regions, where the SABL can develop and persist over several weeks during the polar night. The SABL height is often overestimated, for example, accompanied by excessive turbulent mixing, large surface temperature biases, and erroneous surface energy fluxes and fog formation.

It has been demonstrated, however, that the SABL can be modelled in a realistic way by using a single-column model (SCM) of the atmosphere (e.g., Steeneveld *et al.*, 2006; Baas *et al.*, 2018; Sterk *et al.*, 2015; 2016; Costa *et al.*, 2020), given that the model is provided with appropriate initial state and boundary conditions. An SCM makes use of the same model physics as a mesoscale NWP model, but on a small stencil of just a few horizontal grid points. It can be applied to model a very localised atmospheric column at a high vertical resolution, in a computationally cheap way. As such, SCMs can be run with a very high number of vertical levels, which helps overcome the issues related to applying MOST-based turbulence schemes at a coarse vertical resolution already described herein. Owing to their limited horizontal extent, SCMs are suited best to model weak-advection cases, in which the lateral boundary conditions are easier to formulate and do not completely dominate the model state's evolution. Sterk *et al.* (2013) and Bosveld *et al.* (2014), for example, used SCMs to study the model sensitivity towards thermal conductivity of the top surface layer, long-wave radiation at the ground, and turbulent mixing within the SABL, which represent the three most important contributors to the cooling rate at the ground, which promotes stable stratification (see also Savijärvi and Kauhanen, 2001).

The aim of our study is to guide future research and model development regarding the representation of the SABL in operational NWP models and regional climate simulations. We run a mesoscale NWP model in order to simulate the atmospheric state during the ISOBAR18 campaign (Kral *et al.*, 2021), which took place in February 2018 in Bothnian Bay at Hailuoto Marjaniemi, Finland, and evaluate the model performance regarding the representation of the SABL over snow-covered sea ice. Next, we model the SABL evolution at the ISOBAR18 observation site with an SCM, which receives its boundary conditions from the NWP model. With the computationally cheap SCM, we can analyse the modelled surface fluxes and probe the model sensitivity towards adjustments to very local surface conditions. The NWP model that we use is the open-source Weather Research and Forecasting (WRF) model, both in its three-dimensional mesoscale configuration (hence WRF3D) and in its SCM mode (hence WRFSCM). The unique observational dataset collected during ISOBAR18 captures the observed SABL evolution in a novel combination of meteorological mast data and measurements taken by sodar, lidar, and uncrewed aircraft systems (UASs). These UAS measurements allow for an evaluation of the atmosphere's vertical structure far beyond the range of conventional observations and at a higher vertical resolution. This observational dataset is especially well suited for the evaluation of SCM simulations with a high number of tightly spaced vertical levels, and it provides a unique opportunity to conduct and verify such a real-data model study of the SABL.

Further details about the ISOBAR18 measurement campaign and the observed case study are given in Section 2, together with a description of the sea-ice data from the Finnish Meteorological Institute (FMI) that provide the lower boundary conditions for our model. Our initial WRF3D model runs are described in Section 3. With our results from these experiments we also quantify the outcome of the use of the FMI sea-ice data and two different atmospheric reanalyses as forcing data. The WRFSCM experiments and the model adjustments to local conditions at the ISOBAR18 observation site are presented in Section 4. The conclusions from our study are presented in Section 5, together with a summary of our work.
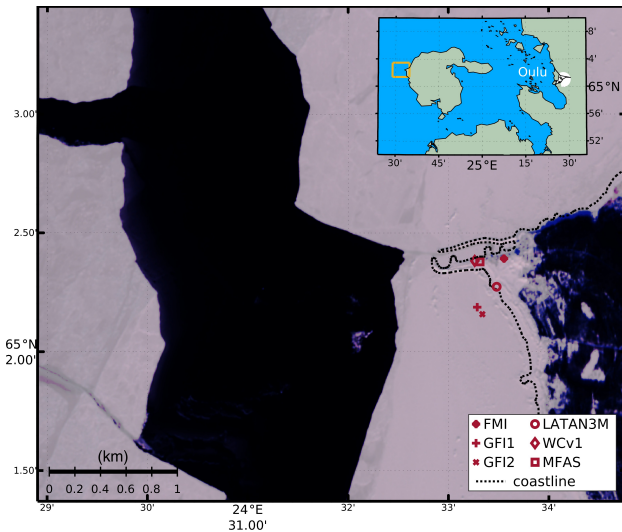
FIGURE 1 Map of the field location during ISOBAR18 close to Hailuoto Marjaniemi. The location of the ground-based instrumentation is indicated as follows. World Meteorological Organization weather station Hailuoto Marjaniemi (Finnish Meteorological Institute, FMI), 2-m micrometeorological mast (GFI1), 10-m micrometeorological mast (GFI2), one-dimensional (vertical-pointing) sodar (LATAN3M), profiling Doppler wind lidar (WCv1), three-dimensional sodar (MFAS). The satellite image displays the local sea ice conditions as observed by Sentinel-2 L1C on February 23, 2018, 101016 UTC (https://apps.sentinel-hub.com/eo-browser)

2 | OBSERVATIONAL DATASET

2.1 | ISOBAR18

ISOBAR18 was the second field campaign of the ISO-BAR project, which employs new observational methods to investigate SABL processes and their representation in numerical models. ISOBAR18 was carried out over the sea ice and coastal regions of the Finnish island Hailuoto during February 2018 (Kral *et al.*, 2021). The island Hailuoto is roughly $200 \, \mathrm{km}^2$ large and is characterised by flat terrain with an elevation of up to 20 m. The field site, located at 65.037°N and 24.555°E, is characterised by a land sector extending clockwise from eastnortheast to southeast, and a sea-ice sector extending clockwise from southeast to eastnortheast, which is interrupted by a 200-m wide pier area of about 5 m elevation to the north (see Figure 1).

Figure 1 shows the locations of the ground-based instrumentation during ISOBAR18. The instrumental set-up and observation strategy were similar to its predecessor, ISOBAR17, which was conducted at the same site (Kral *et al.*, 2018). In addition to the FMI operational weather station Hailuoto Marjaniemi (World Meteorological Organization station ID: 02873), a 10 m micrometeorological mast was installed on the sea ice,

about 500 m southwest of the FMI weather station, labelled GFI2 in Figure 1. This mast was equipped with three eddy-covariance systems (at 2.0, 4.6, and 10.3 m above ground level (agl) and sampling with 20 Hz) and slow-response (1 Hz) instrumentation for temperature, relative humidity, wind speed, and wind direction at 0.6, 2.0, and 6.8 m agl in addition to radiation and ground heat flux measurement systems. A smaller, 2.0-m micrometeorological mast (GFI1) equipped with one eddy-covariance system and radiation instrumentation was installed about 60 m northwest of the 10-m mast.

The installation also included a Doppler wind lidar (WCv1) and a sodar system (MFAS) for vertical profiles of the three-dimensional wind at a spatio-temporal resolution of 20 m every 4 s up to 250 m, and 10 m every 10 min up to 500 m, respectively. A second, vertically pointing sodar (LATAN3M) provided vertical profiles of the vertical velocity and attenuated backscatter every 3 s in 10 m vertical resolution up to 340 m.

In addition to the ground-based observational set-up already described, data sampling during ISOBAR18 relied on airborne UAS measurements based on a variety of systems. In this study, we only make use of kinematic and thermodynamic observations taken with the Small Unmanned Meteorological Observer (SUMO; Reuder *et al.*, 2012). SUMO observations encompassed vertical profiles along a helical flight pattern up to 1800 m agl, which were repeated every 3–4 hr during intensive observational periods (IOPs).

For further details on the measurement systems and the instrumental set-up, we refer to Kral *et al.* (2021).

2.2 | IOP-14

Several IOPs were carried out during ISOBAR18, when conditions were expected to favour very stable stratification (e.g., weak winds and clear sky). We focus our simulation efforts on the SABL evolution during February 23–24, which includes IOP-14 (February 23, 2018, 1615–2030 UTC). The SABL development in this case was driven by radiative cooling at the ground, and the atmospheric stability intensified at sunset, as the long-wave radiative cooling became even more dominant in the surface radiation budget.

The formation of the very stable boundary layer can be seen in the sodar echogram shown in Figure 2, which visualises the vertical structure of the turbulence and thereby the depth of the boundary layer. The boundary-layer height is reduced abruptly at sunset (*im*1400 UTC), from about 200 m down to 50 m, as very stable conditions begin to form and cold air accumulates directly above the ground in the absence of incoming solar radiation. Time series of
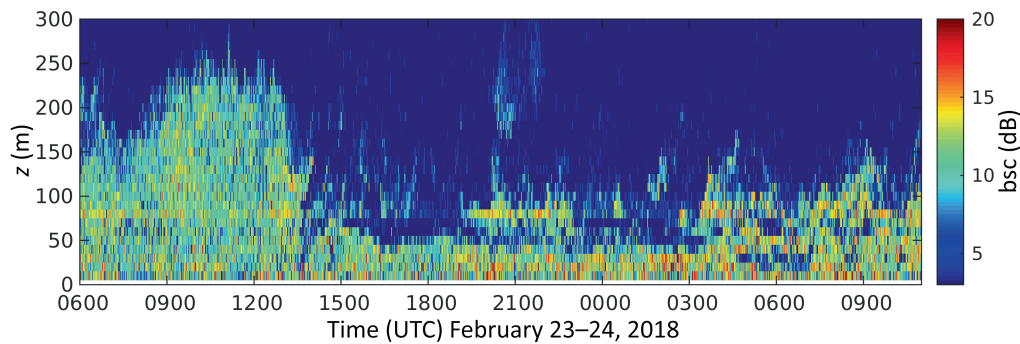
FIGURE 2 Sodar echogram indicating the temporal evolution of the turbulent structure of the stable atmospheric boundary layer during February 23, 2018, 0600 UTC–February 24, 2018, 1100 UTC. bsc: backscatter coefficient

observed radiation fluxes at the surfaces, the ground heat flux, wind speed and air temperature during IOP-14 are shown in the results sections. The observed 10 m wind speed was between 2 and 3 m·s^{-1}, and even dropped down to close to 0 m·s^{-1} towards February 24 0200 UTC. The whole event was characterised by a general cooling of the SABL, with a cooling of about 10 K from noon to night, and an intensification of the surface-based temperature inversion. The SABL prevailed through the night as a nocturnal SABL, and several microfronts (Mahrt, 2019) passed, causing small-scale disturbances in air temperature and turbulence. More details about IOP-14 are given in Kral *et al.* (2021).

During ISOBAR18, the sea ice extent in Bothnian Bay was subject to rapid growth, with a minimum on February 2 and a maximum around February 23 (see Kral *et al.*, 2021, figure 4). This resulted in a continuous sea-ice cover around Hailuoto, which is common in February (Uotila *et al.*, 2015). Sea-ice properties, such as thickness and surface roughness, were of high spatial variability. The modelled surface roughness in the Baltic Sea ranges from 0.0001 to 0.001 m. It is calculated dynamically in open-sea grid points and computed as a function of the snow depth in sea-ice grid points. The actual variability likely was even larger because WRF does not account for sea-ice properties such as ridging and age. Corresponding heterogeneities in the surface temperature field contribute to the complication of local boundary-layer dynamics and thermodynamics.

2.3 | FMI sea-ice charts

In order to make our model set-up comparable to contemporary NWP models employed in Bothnian Bay and Scandinavia, we derive the boundary conditions for sea-ice concentration in our WRF3D model runs from high-resolution sea-ice charts.

The operational sea-ice service at FMI, in collaboration with the Swedish Ice Service, produces sea-ice charts on a daily basis, released at 1200 UTC each day during the Baltic Sea ice season. In addition to graphic charts available at https://en.ilmatieteenlaitos.fi/ice-conditions, gridded versions with different resolutions are produced. These include the following parameters: ice concentration (per cent), average, minimum, and maximum ice thickness (centimetres), degree of ice ridging, and surface temperature (kelvin). In this study, gridded ice-concentration data with 0.5 km resolution are used.

The ice charts are based on manual interpretation of in-situ observations of sea ice conditions (Ronkainen *et al.*, 2018) and satellite data, including synthetic aperture radar images from RADARSAT-2, SENTINEL-1, COSMO-SkyMed, and TerraSAR-X/TanDEM-X satellites. In addition, visual and infrared data from Moderate Resolution Imaging Spectroradiometer and National Oceanic and Atmospheric Administration satellites are used. In-situ observations are from coastal ice observation stations, from Finnish and Swedish icebreakers, pilot vessels, ships, and ports. The quality of the ice charts near Hailuoto can be considered as higher than average because one of the ice observation stations is located there and because of the large number of passing ships reporting ice conditions.

At the time of writing, gridded ice-chart data are used operationally as input for the NWP model HIRLAM, as well as in various marine models in the Baltic Sea: sea-ice model HELMI (HELsinki Multicategory Ice model; Haapala *et al.*, 2005), sea ice (and snow on top of ice) thermodynamics model HIGHTSI (Cheng and Launiainen, 1998; Launiainen and Cheng, 1998; Cheng and Launiainen, 2003), and in the third-generation spectral wave model WAM cycle 4 (Komen *et al.*, 1996), where the ice is coded as land (Tuomi *et al.*, 2011). The gridded sea-ice concentration and ice thickness information from the ice charts are also delivered to Copernicus Marine Environment

FIGURE 3 The three nested domains used in our Weather Research and Forecasting three-dimensional mesoscale model simulations have a grid spacing of 15 km (domain 1), 3 km (domain 2), and 1 km (domain 3). The colour map indicates the orography in the model in metres above sea level. The red star indicates Hailuoto Marjaniemi, the site of the field campaign
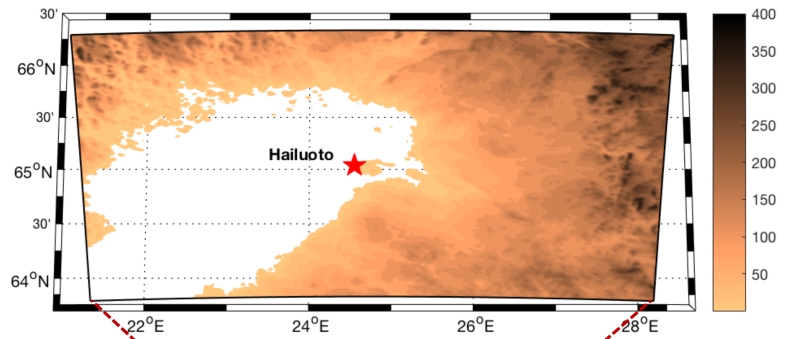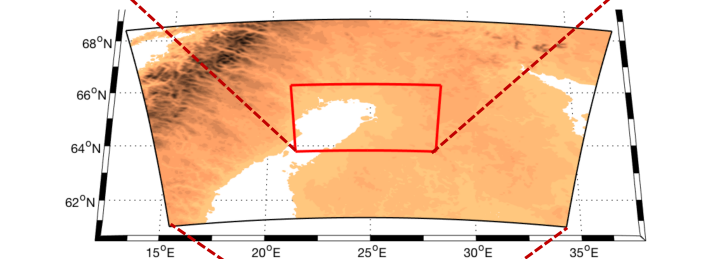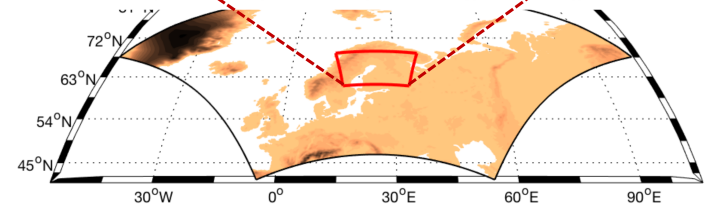
Monitoring Service on a daily basis in a 1 km grid and are available online at http://marine.copernicus.eu/.

3 | MESOSCALE WRF SIMULATIONS: SET-UP, EXPERIMENTAL DESIGN, AND RESULTS

3.1 | WRF3D set-up

The model that we use for our mesoscale NWP studies is the Advanced Research WRF V3.9.1.1 (Skamarock *et al.*, 2008; Powers *et al.*, 2017). We set it up for a dynamical downscaling of a global atmospheric reanalysis at the ISO-BAR18 observation site at Hailuoto (see Section 2), covering the whole of February 2018 and thereby the entire ISOBAR18 campaign. The main objective of the WRF3D simulations is to create a demonstrative example for the typical representation of the SABL in operational NWP models. We also want to use WRF3D output to formulate boundary conditions for SCM experiments on the observation case IOP-14 (see Section 2.2). These WRFSCM experiments are described in the next section. In Section 3.2 we describe the full set of our WRF3D model runs, which is designed to gain further insight into best practice regarding the choice of physical parametrizations and boundary conditions.

The WRF3D simulations are set up with three spatial domains, which are one-way nested into each other and centred on the ISOBAR18 observation site, with a decreasing horizontal grid spacing of 15, 3, and 1 km (see Figure 3). We employ 70 vertical hybrid-pressure levels in each domain, which are terrain-following close to the surface and increasingly isobaric with upper heights. The lowest vertical level is at about 12 m height, which is close to the configuration of operational NWP models. The spacing between levels is approximately 30 m in the lowest kilometre of the atmosphere. It increases gradually until the model top is reached at an atmospheric pressure of 50 hPa. An overview of the model physics common to all WRF3D model runs is given in Table 1.

The WRF3D simulations cover the complete ISO-BAR18 campaign are conducted as continuous model runs, without re-initialisation, ranging from January 30, 2018, 0000 UTC to February 28, 2018, 1800 UTC. Spectral nudging towards the respective driving global reanalysis (i.e., either ERA5 or ERA-Interim; see Section 3.2) is applied to air temperature, horizontal wind components, humidity, and geopotential height in the outermost WRF domain, with WRF's default nudging coefficient of $0.0003\,s^{-1}$. Spectral nudging is only applied above the planetary boundary layer. The horizontal cut-off wavelength for spectral nudging was set to be approximately 1000 km, which follows the recommendation by Gómez and Miguez-Macho (2017).

TABLE 1 Weather Research and Forecasting three-dimensional mesoscale model configuration, including the spatial set-up and the model physics for the three domains shown in Figure 3

	Domain 1	Domain 2	Domain 3
Grid spacing (km)	15	3	1
Extent south–north (grid points)	275	276	277
Extent west–east (grid points)	335	336	334
Time step (s)	45	9	3
Radiation physics	RRTMG (Iacono *et al.*, 2008)		
Microphysics	Thompson (Thompson *et al.*, 2008)		
Land-surface model	Noah LSM (Tewari *et al.*, 2004)		
Cumulus scheme, domain 1 only	Grell3D (Grell and Dévényi, 2002)		

Our WRF configuration makes use of the Noah land-surface model (Tewari *et al.*, 2004) to account for snow-surface–atmosphere coupling, with Moderate Resolution Imaging Spectroradiometer land-use categories. The snow-layer depth on the ground at model initialisation is derived from the global reanalysis data. During the simulation, the snow-layer depth may change based on deposition of snowfall and melting. The snow layer in Noah is modelled as a single-layer snow pack on top of the four soil layers. The sea ice in the Noah land-surface model is partitioned into four vertical layers of 0.75 cm depth each. The sea-ice cover in each grid cell is modelled as a fraction, ranging from 0 to 1. This sea-ice fraction is derived either from the forcing reanalysis (ERA5/ERA-Interim) or from high-resolution sea ice charts, as described below in Section 3.2.

3.2 | WRF3D experimental design

A set of mesoscale WRF simulations is designed to address the following research questions related to the model configuration: (i) determine the most suitable boundary-layer scheme for the study case IOP-14 (see Section 2.1); (ii) quantify the expected advantage of using the high-resolution FMI sea-ice data; (iii) quantify the expected added value from using ERA5 boundary conditions, compared with ERA-Interim.

We perform WRF3D model runs with three different parametrization schemes for the subgrid vertical mixing, the so-called boundary-layer schemes: Mellor–Yamada–Janjić (MYJ; Janjić, 1994), Mellor–Yamada–Nakanishi–Niino (MYNN; Nakanishi and Niino, 2006), and quasi-normal scale elimination (QNSE; Sukoriansky *et al.*, 2005). Each of these schemes works with a turbulence closure of 1.5th order. A detailed comparison of the differences between these schemes is provided by Cohen

et al. (2015). All of these three boundary-layer schemes are, a priori, reasonable choices for mesoscale WRF simulations at either high latitudes or under stable stratification (Mäkiranta *et al.*, 2011; Mayer *et al.*, 2012; Cohen *et al.*, 2015; Tastula *et al.*, 2015; Kim *et al.*, 2019). We want to verify the different WRF3D simulations against observations to determine the best-suited parametrization for air temperature and wind speed during IOP-14, so that we obtain a WRF3D model run that is accurate enough to provide boundary conditions for the SCM experiments on IOP-14 in Section 4.

In addition, we perform WRF3D model runs with initial state and boundary conditions derived from two different global reanalyses from the European Centre for Medium-Range Weather Forecasts (ECMWF): ERA5 and ERA-Interim. ERA5 (Hersbach *et al.*, 2020) is the successor reanalysis of ERA-Interim, and in continuous production at ECMWF. Its one-hourly data describe the global atmospheric state at 0.28125° horizontal resolution. Production of the older ERA-Interim (Dee *et al.*, 2011) was stopped in 2019. ERA-Interim data are six-hourly and have a horizontal resolution of 0.75°. Although ERA-Interim has been commonly replaced by the ERA5 reanalysis in operational settings, we still include a few WRF3D runs driven by ERA-Interim in our experiments because this reanalysis has been in use for such a long time and by so many studies. This allows us to quantify the expected gain in model performance from the higher frequency, resolution, and overall data quality in ERA5.

In order to account for the prevailing heterogeneous sea-ice conditions in Bothnian Bay (see Section 2.2) and to provide our WRF3D simulations with a certain advantage over a standard mesoscale WRF downscaling, the majority of the WRF3D simulations are initialised and forced with high-resolution sea-ice concentration data from the FMI (see Section 2.3), replacing the coarser sea-ice data that
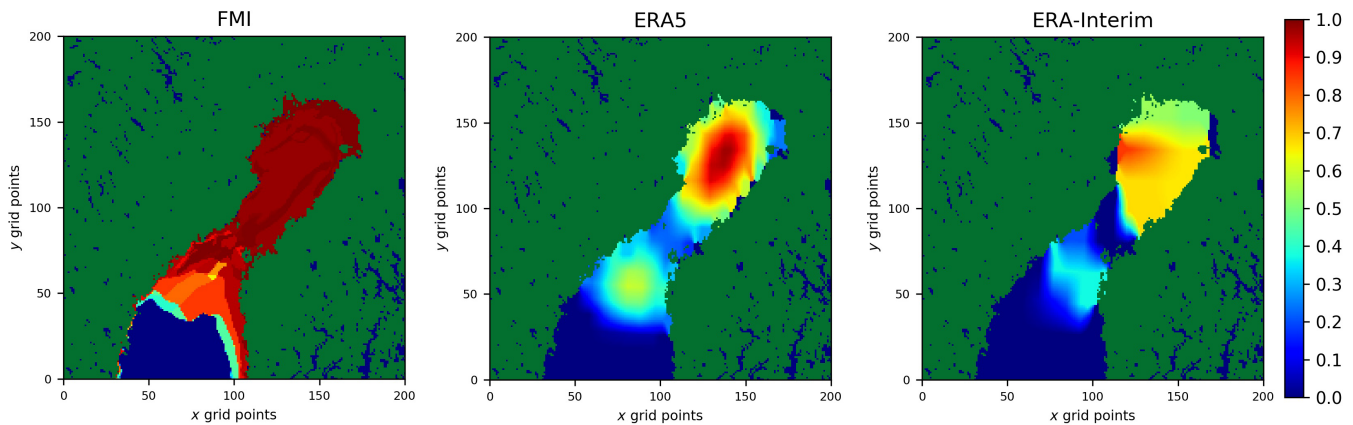
FIGURE 4 Fractional sea-ice concentration in Bothnian Bay in Weather Research and Forecasting domain 2 (see Figure 3), February 24, 2018, 0000 UTC, as derived from Finnish Meteorological Institute (FMI) sea-ice charts (left), ERA5 (centre), and ERA-Interim (right). Land is shown in green and open sea in blue

come with ERA-Interim and ERA5. These high-resolution sea-ice charts are available daily, and a linear interpolation in time is made to obtain sea-ice data of the same frequency as the driving global reanalysis.

Sample fields of sea-ice concentration in WRF3D derived from the FMI ice charts, ERA5, and ERA-Interim are shown in Figure 4. The sea-ice concentrations derived from ERA5 and ERA-Interim show a certain patchiness, which is most likely caused by a combination of insufficient spatial resolution and inadequate default interpolation methods in WRF. The sea-ice concentrations derived from the FMI ice charts, on the other hand, show a much more appropriate extent with physically plausible, fine-scale details.

In summary, our complete set of nine WRF3D model runs is composed as follows. Simulations with three different boundary-layer schemes are made: MYJ, MYNN, and QNSE. For each boundary-layer scheme, we make one model run with initial and boundary conditions from the ERA5 reanalysis and one for ERA-Interim. The sea-ice concentration in all of these simulations is derived from the high-resolution FMI sea-ice data. Finally, the three ERA5 model runs are also conducted with the original ERA5 sea-ice data instead of the FMI ice data. The results from these latter three simulations serve as a reference in quantifying the expected benefits from using the high-resolution FMI sea-ice data.

3.3 | WRF3D results

The performance of the WRF3D simulations is evaluated by comparison of model results from the innermost domain against measurements from the 10-m mast situated south of the pier at Hailuoto Marjaniemi (labelled

GFI2 in Figure 1). Results from this comparison are listed in Table 2. We present a rather simple and short model evaluation because, at this stage, we are mostly interested in which of the WRF3D runs is best suited to provide initial and boundary conditions for the following WRFSCM experiments at the ISOBAR18 observation site. More detailed time-series plots and vertical profiles of this WRF3D model run are shown together with the WRF-SCM output in Section 4. We are also positive that such a brief model evaluation is sufficient to confirm the expected advantage of ERA5 over ERA-Interim and of the FMI ice charts over the default ERA5 sea ice.

From Table 2 we can see that forcing the WRF3D simulations with ERA5 yields better scores for air temperature and wind speed than the use of ERA-Interim, with only a few exceptions. The use of the newer ERA5 reanalysis is certainly advisable in this case. Even more important than the higher spatial and temporal resolution in the forcing reanalysis is the use of the FMI sea-ice charts. The high-resolution sea-ice data greatly enhance the detail at the lower boundary of the simulations, as for example shown in Figure 4, and the scores in Table 2 improve accordingly.

The best scores are achieved by the simulations with ERA5 forcing, FMI sea ice, and either the MYNN or QNSE boundary-layer scheme. The MYNN + ERA5 WRF3D run has the smallest deviation from the observations at the very beginning of the IOP-14 study period, whereas the QNSE + ERA5 WRF3D run has initial biases of about +3 K and +1 m·s^{-1} (not shown). Based on these results, we have made the decision to initialise the WRFSCM simulations with boundary conditions from the MYNN + ERA5 WRF3D simulation and to conduct the WRFSCM simulations with the MYNN surface and boundary-layer schemes.

TABLE 2 Verification scores of the Weather Research and Forecasting three-dimensional mesoscale model simulations with different boundary-layer parameterizations, forcing reanalysis, and sea ice data. Scores are computed against measurements of air temperature at 2 m ($T_{2\,m}$) and wind speed at 10 m height ($U_{10\,m}$), based on hourly model output during the IOP-14 study period February 23, 2018, 0800 UTC–February 24, 2018, 1100 UTC. The best value for each score is highlighted in bold font

	$T_{2\,m}$ RMSE (K)/$T_{2\,m}$ bias (K) $U_{10\,m}$ RMSE (m·s^{-1})/$U_{10\,m}$ bias (m·s^{-1})		
	MYJ	**MYNN**	**QNSE**
ERA-Interim with FMI sea ice	3.67 / 1.99	3.83 / 1.55	3.65 / −1.82
	2.18 / 1.04	2.09 / 1.33	2.71 / 1.87
ERA5 without FMI sea ice	3.83 / 3.00	6.77 / 5.72	7.82 / 6.56
	2.92 / 2.10	3.82 / 3.21	3.03 / 2.53
ERA5 with FMI sea ice	4.55 / −0.95	**1.97** / −1.47	2.23 / **−0.62**
	2.91 / 1.69	1.54 / **0.66**	**1.50** / 1.09

Note: FMI: Finnish Meteorological Institute; MYJ, Mellor–Yamada–Janjić MYNN, Mellor–Yamada–Nakanishi–Niino; QNSE, quasi-normal scale elimination; RMSE, root-mean-square error.

4 | WRFSCM: SET-UP, EXPERIMENTAL DESIGN, AND RESULTS

4.1 | WRFSCM set-up

WRFSCM offers the same physics as the full WRF model, while running on a stencil of 3×3 grid points. Owing to this small spatial domain, the model can be configured with as many as 200 vertical sigma-levels between the surface and the model top at 12 km height, at very low computational costs. In our set-up, the lowest model level is at 0.54 m, which is much lower than the WRF3D set-up and will assist resolving steep vertical gradients. The WRFSCM is running with a substantially increased vertical resolution compared with the WRF3D simulations, especially close to the ground. In the lowest 500 m of the atmosphere, there are 99 WRFSCM levels in our set-up, compared witho merely 16 vertical levels in the WRF3D set-up.

A successful simulation of SABL evolution demands a high accuracy in the prescribed surface parameters to match the very local conditions at the observation site (e.g., Savijärvi and Kauhanen, 2001; Sterk *et al.*, 2015; Baas *et al.*, 2018). The surface in WRFSCM is set to be completely covered by sea ice with a sea-ice thickness of 0.5 m, as derived from the FMI sea-ice charts. Snow pack parameters, such as snow cover, snow height, and snow water equivalent, are adopted from the MYNN + ERA5 WRF3D simulation (see Section 3.3). For IOP-14 (see Section 2.2), these parameters were found to be in good agreement with the observations. According to the observations, the sea ice at the observation site was fully covered by a snow cover of approximately 14 cm depth.

4.2 | WRFSCM experimental design

The key features of the experimental design presented in this section are the treatment of initial and boundary conditions, the definition of a WRFSCM reference simulation based on an analysis of surface energy fluxes, and the strategy behind the WRFSCM simulations with different number of vertical levels.

Even though we select a study case with clear sky, weak wind speeds, and relatively weak advection, in order to minimise the importance of non-local processes, the accuracy of the WRFSCM simulations will depend strongly on the right boundary conditions and forcing data. The initial state of the atmosphere in WRFSCM is adapted directly from the WRF3D output. During runtime, the WRFSCM is forced by hourly updated geostrophic wind U_g and advection of momentum, temperature, and humidity. These hourly forcings are computed from the WRF3D output as well.

Following the approach by Sterk *et al.* (2015) to approximate the geostrophic wind in time and vertically, the components of U_g, from the lowest vertical level up to a certain threshold height z_t, are set equal to the actual wind components from the WRF3D simulation at z_t. Above z_t, U_g is set equal to the actual wind at each individual level. This threshold height z_t has to be above the planetary boundary layer and any potential low-level jet, in order to avoid a too strong U_g at the surface. For Sterk *et al.* (2015), z_t was between 300 and 400 m height. In our case, z_t is at around 600 m height, due to the presence of a strong low-level jet in the WRF3D simulations during the study period.

We then adjust the WRFSCM to site-specific conditions, to define a configuration that serves as a control simulation in the upcoming experiments. These adjustments are based on an analysis of surface energy fluxes

FIGURE 5 Modelled and observed incoming and net short-wave radiation at the ground during February 23, 2018, 0900 UTC–February 24, 2018, 1100 UTC. Observations are from the GFI1 mast. WRF3D: Weather Research and Forecasting three-dimensional mesoscale model; WRFSCM: Weather Research and Forecasting single-cell model; OBS: observations
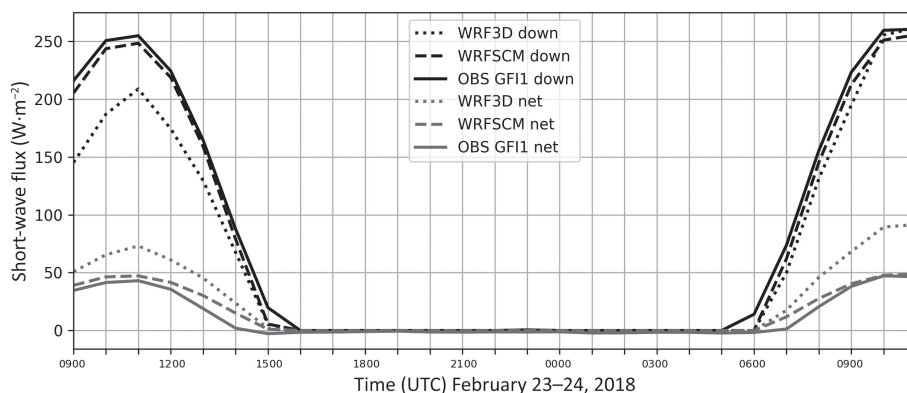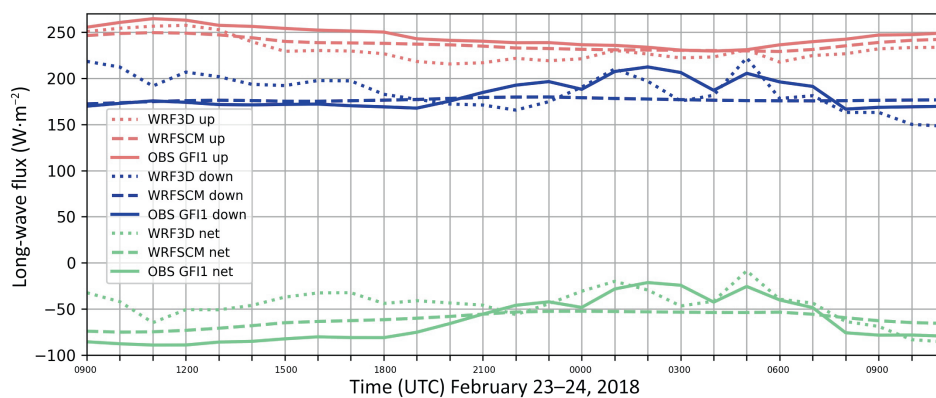

FIGURE 6 As Figure 5, but for upwelling, downwelling, and net long-wave radiation. WRF3D: Weather Research and Forecasting three-dimensional mesoscale model; WRFSCM: Weather Research and Forecasting single-cell model; OBS: observations

in both WRF3D and WRFSCM. This is done to ensure that the critical processes contributing to the SABL evolution are modelled correctly in WRFSCM. This analysis, the resulting WRFSCM control simulation, and an evaluation of near-surface variables in WRF3D and WRFSCM are presented in Section 4.3.1.

Once a WRFSCM control simulation is defined and its near-surface parameters are validated, we run a set of simulations to probe how many vertical levels are needed to simulate vertical profiles as they were observed during IOP-14. The control simulation is run with 200 vertical levels, which is the maximum possible in the official WRF-SCM code. This number of vertical levels allows us to validate the actually modelled 2 m air temperature in WRF-SCM in Section 4.3.1, as opposed to WRF3D where we have to validate a diagnostic 2 m air temperature because its lowest model level is placed too far from the ground (see Section 3.1). The number of vertical levels is then gradually decreased down to 70 (the vertical resolution of the WRF3D simulations), and beyond, down to 50. We leave the exact spacing between the vertical levels to the WRF model, which by default strives for a tighter spacing of levels close to the ground, which is necessary to resolve strong gradients in the SABL (e.g., Steeneveld *et al.*, 2006; Costa *et al.*, 2020). These experiments and the evaluation against the observed vertical profiles are presented in Section 4.3.2.

4.3 | WRFSCM results

4.3.1 | Surface fluxes and near-surface evaluation

In this section, we validate surface energy fluxes at the ISOBAR18 observation site from the MYNN + ERA5 mesoscale WRF simulation (see Section 3.3), which is from now on simply referred to as WRF3D, and from WRFSCM against observations made during IOP-14. We do this to ensure that these fluxes are modelled correctly in all subsequent WRFSCM simulations. Afterwards, we show and discuss the near-surface wind speed and air temperature in WRF3D and WRFSCM.

First, we illustrate the SABL evolution during IOP-14 with time series of modelled and observed surface radiation fluxes (Figures 5 and 6). From Figures 5 and 6, we can identify two important processes contributing to the formation of very stable conditions during the afternoon of IOP-14: the steadily decreasing net short-wave flux (reaching 0 W·m^{-2} at sunset), and the constant radiative long-wave cooling at the surface (snow-covered sea ice). In WRF3D, the modelled net long-wave radiation is about 40–50 W·m^{-2} too high in the first half of the study period. This is because WRF3D produces a too thick and persistent fog close to the ground (identified in the model output as too high cloud-fraction, not shown), which traps
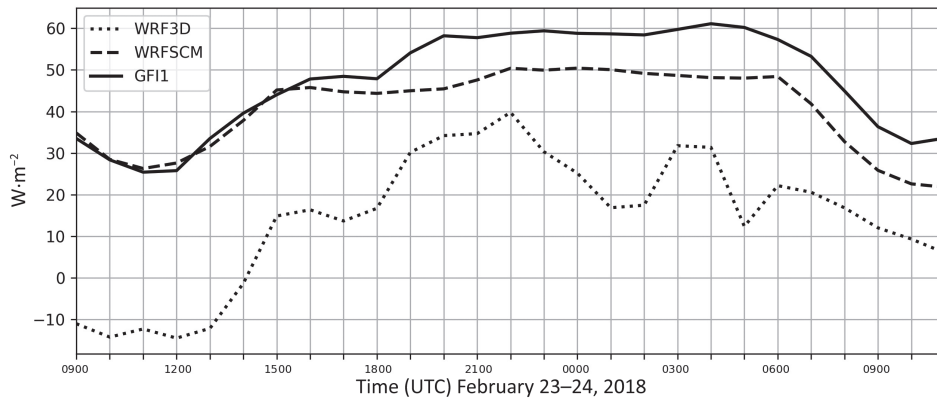
FIGURE 7 As Figure 5, but for upward ground heat flux within the snow layer. WRF3D: Weather Research and Forecasting three-dimensional mesoscale model; WRFSCM: Weather Research and Forecasting single-cell model
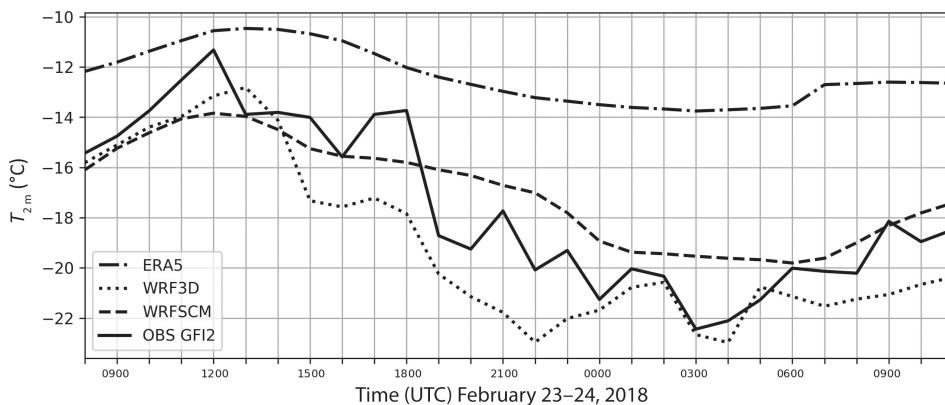

FIGURE 8 Time series of modelled and observed 2 m air temperature at the 10-m mast on the sea ice during February 23, 2018, 0800 UTC–February 24, 2018, 1100 UTC. WRF3D: Weather Research and Forecasting three-dimensional mesoscale model; WRFSCM: Weather Research and Forecasting single-cell model; OBS: observations

long-wave radiation emitted at the surface. In order to correct the long-wave radiation budget at the surface in WRFSCM, we multiply the initial humidity profile by a factor of 0.5. This follows the approach by Sterk *et al.* (2016), who demonstrated how the long-wave radiation budget under such conditions is mostly dependent on the humidity in the atmospheric column. The resulting long-wave radiation in WRFSCM is consequently in good agreement with the observed values (see Figure 6), especially during daytime.

The net short-wave flux in the WRF3D simulation is too large, even though the corresponding incoming solar radiation is too low (see Figure 5). This is partly because the excessive atmospheric humidity in WRF3D (see earlier herein) blocks incoming solar radiation. In addition, the default sea-ice albedo of 0.65 in WRF3D is too low compared with the observed albedo, which was about 0.85 averaged over the duration of IOP-14. We have subsequently set the surface albedo for all WRFSCM simulations to 0.81, in order to optimise the net short-wave flux and to compensate for an incoming solar radiation in WRFSCM that is slightly lower than observed (see Figure 5). This value is, for example, also very close to that by Hines *et al.* (2015), who use an albedo of 0.82 for wintertime sea ice.

As a final measure in defining the configuration for the WRFSCM control simulation, we investigate the ground heat flux G at the surface. Figure 7 shows a time series of G over the study period. In WRF3D, the modelled ground heat flux is consistently too low, by about 20–40 $W \cdot m^{-2}$. Most of this bias in G is removed in WRFSCM, which is almost exclusively due to the adjusted sea-ice thickness of 0.5 m (see Section 4.1), compared with the default sea-ice thickness in WRFs Noah land-surface model of 3.0 m (see Section 3.1).

Now that the surface radiation budget and ground heat flux are modelled in much better approximation in the SCM, the configuration of the WRFSCM control simulation is completed. We proceed with an evaluation of near-surface air temperature and wind speed. The cooling of the near-surface air during the nocturnal SABL evolution is clearly visible in the time series of 2 m air temperature (Figure 8). The plot shows that the 2 m air temperature in both WRF3D and WRFSCM is relatively close to the observations during most of the simulation. Overall, WRFSCM is subject to a slight positive temperature bias, whereas there is a cold temperature bias in WRF3D. WRF3D captures the temperature minimum during the night better, which WRFSCM misses by about 2.5 K. Table 3 shows that WRFSCM performs slightly better in terms of root-mean-square error (RMSE) and bias, averaged over the whole study period.

TABLE 3 Verification scores for near-surface parameters in ERA5, WRF3D (MYNN + ERA5) and WRFSCM. Scores are computed against measurements of air temperature at 2 m ($T_{2\,m}$) and wind speed at 10 m (U_{10m}) from the GFI2 mast, based on hourly model output during February 23, 2018, 0800 UTC–February 24, 2018, 1100 UTC

	T_{2m} RMSE (K)	T_{2m} bias (K)	$U_{10\,m}$ RMSE (m·s^{-1})	U_{10m} bias (m·s^{-1})
ERA5	5.63	5.17	1.88	1.73
WRF3D	1.97	−1.47	1.54	0.66
WRFSCM	1.73	0.63	0.71	−0.11

Note: MYNN, Mellor–Yamada–Nakanishi–Niino; RMSE, root-mean-square error; WRF3D, weather research and forecasting three-dimensional mesoscale model; WRFSCM, weather research and forecasting single-cell model.

Whereas the time series of 10 m wind speed in WRF3D (Figure 9) varies erratically between 1 and 6 m·s^{-1}, the time series of wind speed in WRFSCM is much smoother. The lower variability in WRFSCM stems likely from the smoothed, hourly geostrophic wind forcing and momentum advection, whereas the wind in WRF3D is a product of several instantaneous dynamical and physical processes in superposition. The values of RMSE and bias of 10 m wind speed are lower for WRFSCM than for WRF3D (see Table 3).

The values from the ERA5 reanalysis are included in Figures 8 and 9 as well. These values are taken from the closest ERA5 grid point, a land point with a snow cover of 100% and a snow depth of 34 cm, and no spatial interpolation is applied. We have also looked into values from the closest ERA5 ocean grid point, one grid point to the west, with a sea-ice concentration of 54%: differences in 2 m temperature between both ERA5 grid points are <1 K, and for our results it does not matter which ERA5 grid point is used. The 2 m temperature in ERA5 is characterised by a large positive bias throughout the study period. The observed temperature minimum is missed by more than 8 K. There is also a discontinuity in the temperature

time-series at 0700 UTC on February 24, 2018. In general, the temperature in ERA5 shows a much lower variability than that in WRF3D and WRFSCM. The values for 10 m wind speed in ERA5 are also larger than the observations. It is also noteworthy that both variables have a large initial bias, at the beginning of the study period. This demonstrates the need for the downscalings with WRF3D to obtain adequate initial conditions for the WRFSCM experiments.

We proceed with a more detailed description of the SABL evolution during IOP-14 and an evaluation of the vertical structure of the modelled SABL in WRF3D and WRFSCM in the following subsection.

4.3.2 | Vertical resolution and evaluation of profiles

We evaluate the vertical build-up of the atmosphere in the various model runs by a comparison with vertical profiles observed by the UAS SUMO (see Section 2). During IOP-14, SUMO undertook four vertical profile flights, at 1728 UTC and 2115 UTC on February 23, 2018, and at 0115 UTC and 0509 UTC on February 24, 2018. We show measurements of potential temperature (see Figure 10) and wind speed (Figure 11) from these flights, together with model output from WRF3D and WRFSCM, and observed wind speed from the Doppler wind lidar (marked "WCv1" in Figure 1). From WRFSCM, we show output from the reference run with 200 vertical levels, and output from WRFSCM with 70 (same amount as WRF3D) and 50 vertical levels.

The upper part of the SABL, in which the potential temperature increases with height, is visible in all four SUMO potential temperature profiles. The transition from the SABL to the residual layer above, with a constant potential temperature with height, takes place at a height of 80–100 m. The inversion at the ground is clearly visible in all WRFSCM profiles. Though the exact transition

FIGURE 9 As Figure 8, but for 10 m wind speed. WRF3D: Weather Research and Forecasting three-dimensional mesoscale model; WRFSCM: Weather Research and Forecasting single-cell model; OBS: observations
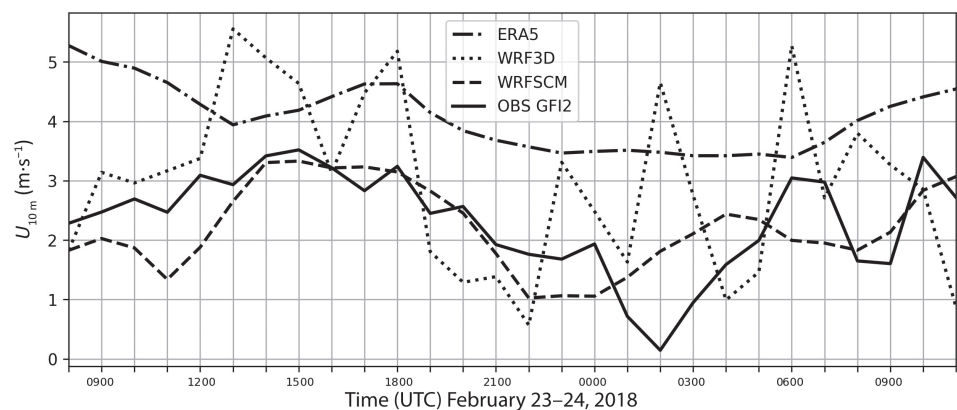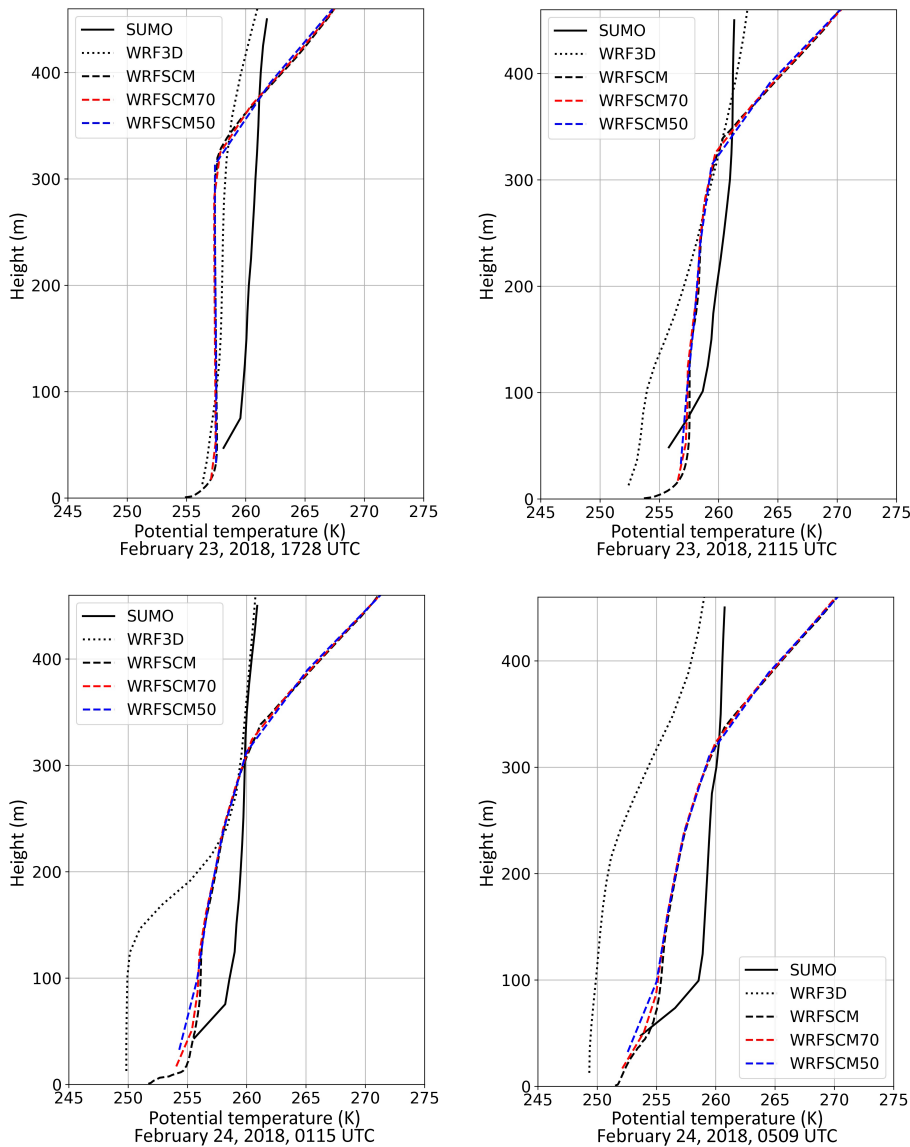
FIGURE 10 Modelled and observed vertical profiles of potential temperature. Date and time are indicated below each panel. Model output is taken from the closest full hour. SUMO: Small Unmanned Meteorological Observer; WRF3D: Weather Research and Forecasting three-dimensional mesoscale model; WRFSCM: Weather Research and Forecasting single-cell model

between the SABL and the layer of neutral potential temperature above is difficult to identify, it seems that WRFSCM produces an SABL that is rather too shallow, compared with the observations. The profiles from WRF-SCM also contain an inversion starting at around 300 m that has not been observed as such. This inversion is inherited from the initialisation data derived from WRF3D, and it persists in WRFSCM, whereas it dissolves over time in WRF3D. It is noteworthy, however, that WRFSCM is clearly able to create stable conditions at the ground, whereas the potential temperature profiles in WRF3D are much less stable. In particular, the WRF3D profile at 0115 UTC on February 24, 2018, shows an almost neutral stratification at the ground with a capping inversion on top of it. Overall, WRF3D is subject to a cold temperature bias, which amplifies over time. The potential temperature in WRFSCM is in general closer to the observations, especially in the two profiles from February 24, 2018.

Differences between the WRFSCM runs with different number of vertical levels are, naturally, most visible where there are gradients in the potential temperature; that is, within the SABL and in the upper-air inversion. The differences are not large. In the SABL, the potential temperatures in the runs with fewer vertical levels are lower than in the WRFSCM reference run.

The observed wind-speed profiles are mostly constant with height, and the overall wind speed decreases over the course of IOP-14. At 2115 UTC on February 23, 2018, a low-level jet with its wind speed maximum at 100 m is visible, both in the SUMO and the lidar observations. The same jet is present in the first profile as well, truncated by missing data at lower heights in SUMO, but well resolved by the lidar. Wind speeds from WRF-SCM are generally closer to the observations than those from WRF3D, especially in the first 100–200 m above the ground. None of the models, however, contain a low-level

FIGURE 11 As Figure 10, but for wind speed. SUMO: Small Unmanned Meteorological Observer; WRF3D: Weather Research and Forecasting three-dimensional mesoscale model; WRFSCM: Weather Research and Forecasting single-cell model
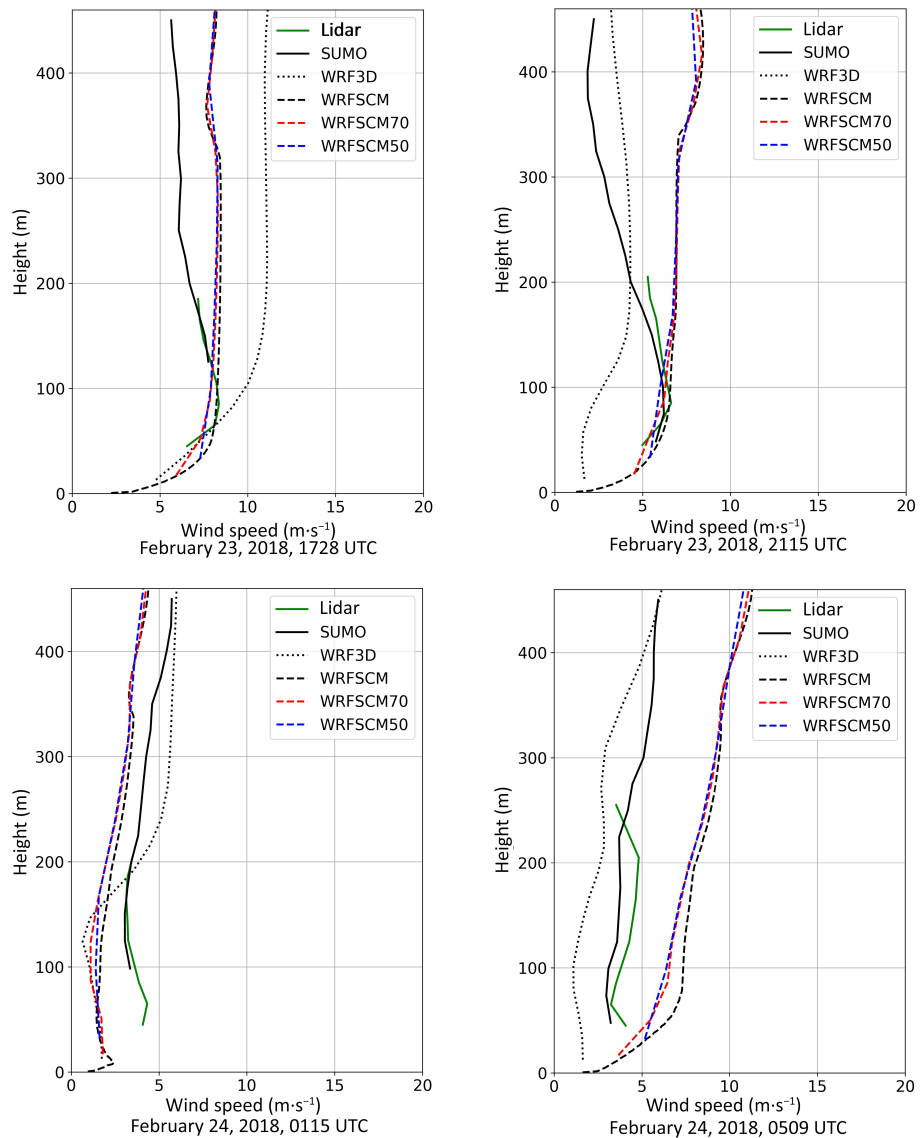
jet, as is observed in the first two profiles. At upper heights of 300–400 m, WRF3D is more accurate than WRFSCM. The fourth wind-speed profile is modelled particularly well in WRF3D.

As with potential temperature, differences between the WRFSCM runs with different amount of vertical levels are not large and most pronounced in the lowest 100 m. The model runs with fewer vertical levels produce lower wind speeds.

5 | SUMMARY AND CONCLUSIONS

We apply the WRFSCM to simulate an SABL evolution that was observed during the ISOBAR18 measurement campaign at the Finnish island Hailuoto in Bothnian Bay, northern Europe (Figure 1). Boundary conditions for the WRFSCM simulations are derived from a set of mesoscale

WRF simulations (WRF3D). In these WRF3D simulations, the global reanalyses ERA5 and ERA-Interim are gradually downscaled to a grid spacing of 1 km (Table 1 and Figure 3). The WRF3D simulations are evaluated against ISOBAR18 measurements (Table 2), and we find that downscaling the ERA5 reanalysis, with its increased temporal and spatial resolution, provides the best results. In addition, we derive the sea-ice concentration boundary conditions for WRF3D from daily sea-ice maps from the FMI. This greatly enhances the representation of the prevailing sea-ice cover in the model (Figure 4), and the verification scores of near-surface wind and temperature are drastically improved by the use of the FMI ice charts over the original sea-ice concentration from the ERA5 reanalysis (Table 2).

The WRFSCM is set up for a simulation period of February 23, 2018, 0800 UTC to February 24, 2018, 1000 UTC in order to cover IOP-14 (Kral et al., 2021),

during which an SABL over snow-covered sea ice transitioned to very stable conditions, accompanied by cold-air advection and passing microfronts. Biases in the surface heat fluxes that are present in WRF3D are corrected in WRFSCM (see Figures 5–7) by adjusting the local humidity profile, snow albedo, and sea-ice thickness (see Section 4.3.1). Time series of near-surface temperature and wind speed from this WRFSCM configuration (Figures 8 and 9) score well against mast measurements at the observation site, in terms of bias and RMSE (Table 3). The scores in Table 3 also demonstrate the necessity and validity of our downscaling approach, as the 2-m-temperature RMSE in ERA5 of 5.6 K is reduced to 1.7 K in WRFSCM. While WRFSCM is subject to a slight warm temperature bias and misses the observed temperature minimum, WRF3D has a larger, cold temperature bias. It is noteworthy, however, that scores from WRF3D are not inherently bad, even though WRF3D differs so strongly from WRFSCM in terms of the modelled surface energy fluxes.

Our study emphasises the necessity of high-quality in-situ observations, especially for modelling approaches such as ours, which aim to represent individual processes like radiative cooling and ground heat flux separately, instead of combining them into an idealised surface cooling rate (e.g., see Costa *et al.*, 2020). Without such observations, good verification scores of near-surface variables may easily be attributed to the wrong physical processes, whereas the ISOBAR18 observations have enabled us to identify and rectify deficiencies in the modelled radiation budget and ground heat flux. Further, this study highlights the delicate balance of processes involved in SABL evolution, in which a change for the better in the modelling of one process may easily tip the overall model performance to being worse.

Earlier studies have shown that an SCM is capable of simulating SABL evolution to a rather high degree of accuracy, provided there are accurate boundary conditions, while stressing the necessity of a high number of vertical levels, especially at the boundaries (e.g., Steeneveld *et al.*, 2006; Costa *et al.*, 2020). Our study confirms this. In our case, adding more vertical levels does not solve categorical issues like the missing low-level jet (Figure 11), but this does help with the overall amplitude of the potential temperature gradient in the SABL (Figure 10) and adding details to the representation of such steep gradients.

In conclusion, our study makes a very strong case for the consideration of higher quality sea-ice thickness and albedo information in NWP and climate models, and atmospheric reanalysis data sets. Including sea-ice thickness as a variable in ERA5, for example, would be a great service to the NWP and regional climate modelling community, to make this critical information widely and publicly available to research groups and operational agencies.

ORCID
T. Lorenz https://orcid.org/0000-0003-2584-4915
I. Suomi https://orcid.org/0000-0002-2523-3252
G.-J. Steeneveld https://orcid.org/0000-0002-5922-8179

REFERENCES
Atlaskin, E. and Vihma, T. (2012) Evaluation of NWP results for wintertime nocturnal boundary-layer temperatures over Europe and Finland. *Quarterly Journal of the Royal Meteorological Society*, 138, 1440–1451.

Baas, P., Van De Wiel, B.J.H., van der Linden, S.J.A. and Bosveld, F.C. (2018) From near-neutral to strongly stratified: Adequately modelling the clear-sky nocturnal boundary layer at Cabauw. *Boundary-Layer Meteorology*, 166, 217–238.

Bosveld, F.C., Baas, P., Steeneveld, G.-J., Holtslag, A.A., Angevine, W.M., Bazile, E., de Bruijn, E.I.F., Deacu, D., Edwards, J.M., Ek, M., Larson, V.E., Pleim, J.E., Raschendorfer, M. and Svensson, G. (2014) The third GABLS intercomparison case for evaluation studies of boundary-layer models. Part B: Results and process understanding. *Boundary-Layer Meteorology*, 152, 157–187.

Cheng, B. and Launiainen, J. (1998). A one-dimensional thermodynamic air–ice–water model: Technical and algorithm description report (MERI—Report Series of the Finnish Institute of Marine Research, No. 37), pp. 15–35. Helsinki, Finland: Finnish Institute of Marine Research.

Cheng, B., Vihma, T. and Launiainen, J. (2003) Modelling of superimposed ice formation and subsurface melting in the Baltic Sea. *Geophysica*, 39, 31–50.

Cohen, A.E., Cavallo, S.M., Coniglio, M.C. and Brooks, H.E. (2015) A review of planetary boundary layer parameterization schemes and their sensitivity in simulating southeastern U.S. cold season severe weather environments. *Weather and Forecasting*, 30, 591–612.

Costa, F.D., Acevedo, O.C., Medeiros, L.E., Maroneze, R., Puhales, F.S., Carvalho Jr., A.D., Camponogara, L.F., dos Santos, D.M. and Mortarini, L. (2020) Stable boundary layer regimes in single-column models. *Journal of the Atmospheric Sciences*, 77, 2039–2054.

Davy, R. and Esau, I. (2016) Differences in the efficacy of climate forcings explained by variations in atmospheric boundary layer depth. *Nature Communications*, 7, 11690.

Dee, D.P., Uppala, S.M., Simmons, A.J., Berrisford, P., Poli, P., Kobayashi, S., Andrae, U., Balmaseda, M.A., Balsamo, G., Bauer, P., Bechtold, P., Beljaars, A.C.M., Van de Berg, L., Bidlot, J., Bormann, N., Delsol, C., Dragani, R., Fuentes, M., Geer, A.J., Haimberger, L., Healy, S.B., Hersbach, H., Hólm, E.V., Isaksen, L., Ka·llberg, P., Köhler, M., Matricardi, M., McNally, A.P., Monge-Sanz, B.M., Morcrette, J.-J., Park, B.-K., Peubey, C., de Rosnay, P., Tavolato, C., Thépaut, J.-N. and Vitart, F. (2011) The ERA-Interim reanalysis: Configuration and performance of the data assimilation system. *Quarterly Journal of the Royal Meteorological Society*, 137, 553–597.

Gómez, B. and Miguez-Macho, G. (2017) The impact of wave number selection and spin-up time in spectral nudging. *Quarterly Journal of the Royal Meteorological Society*, 143, 1772–1786.

Grell, G.A. and Dévényi, D. (2002) A generalized approach to parameterizing convection combining ensemble and data assimilation techniques. *Geophysical Research Letters*, 29, 38–1–38-4.

Haapala, J., Lönnroth, N. and Stössel, A. (2005) A numerical study of open water formation in sea ice. *Journal of Geophysical Research: Oceans*, 110, C09011.

Hersbach, H., Bell, B., Berrisford, P., Hirahara, S., Horányi, A., Muñoz-Sabater, J., Nicolas, J., Peubey, C., Radu, R., Schepers, D., Simmons, A., Soci, C., Abdalla, S., Abellan, X., Balsamo, G., Bechtold, P., Biavati, G., Bidlot, J., Bonavita, M., Chiara, G., Dahlgren, P., Dee, D., Diamantakis, M., Dragani, R., Flemming, J., Forbes, R., Fuentes, M., Geer, A., Haimberger, L., Healy, S., Hogan, R.J., Hólm, E., Janisková, M., Keeley, S., Laloyaux, P., Lopez, P., Lupu, C., Radnoti, G., Rosnay, P., Rozum, I., Vamborg, F., Villaume, S. and Thépaut, J.-N. (2020) The ERA5 global reanalysis. *Quarterly Journal of the Royal Meteorological Society*, 146, 1999–2049.

Hewson, T. (2019). Use and verification of ECMWF products in member and co-operating states (2018) (ECMWF Technical Memorandum No. 840). Reading, UK: ECMWF.

Hines, K.M., Bromwich, D.H., Bai, L., Bitz, C.M., Powers, J.G. and Manning, K.W. (2015) Sea ice enhancements to polar WRF. *Monthly Weather Review*, 143, 2363–2385.

Holtslag, A.A.M., Svensson, G., Baas, P., Basu, S., Beare, B., Beljaars, A.C.M., Bosveld, F.C., Cuxart, J., Lindvall, J., Steeneveld, G.J., Tjernström, M. and Van De Wiel, B.J.H. (2013) Stable atmospheric boundary layers and diurnal cycles: Challenges for weather and climate models. *Bulletin of the American Meteorological Society*, 94, 1691–1706.

Iacono, M.J., Delamere, J.S., Mlawer, E.J., Shephard, M.W., Clough, S.A. and Collins, W.D. (2008) Radiative forcing by long-lived greenhouse gases: Calculations with the AER radiative transfer models. *Journal of Geophysical Research: Atmospheres*, 113, D13103.

Janjić, Z.I. (1994) The step-mountain eta coordinate model: Further developments of the convection, viscous sublayer, and turbulence closure schemes. *Monthly Weather Review*, 122, 927–945.

Kim, D.-H., Kim, H.M. and Hong, J. (2019) Evaluation of wind forecasts over Svalbard using the high-resolution Polar WRF with 3DVAR. *Arctic, Antarctic, and Alpine Research*, 51, 471–489.

Komen, G.J., Cavaleri, L., Donelan, M., Hasselmann, K., Hasselmann, S. and Janssen, P.A.E.M. (1996) *Dynamics and modelling of ocean waves*. Cambridge, UK: Cambridge University Press.

Kral, S.T., Reuder, J., Vihma, T., Suomi, I., Haualand, K.F., Urbancic, G.H., Greene, B.R., Steeneveld, G.-J., Lorenz, T., Maronga, B., Jonassen, M.O., Ajosenpää, H., Båserud, L., Chilson, P.B., Holtslag, A.A.M., Jenkins, A.D., Kouznetsov, R., Mayer, S., Pillar-Little, E.A., Rautenberg, A., Schwenkel, J., Seidl, A. and Wrenger, B. (2021) The innovative strategies for observations in the Arctic Atmospheric Boundary Layer Project (ISOBAR)—Unique fine-scale observations under stable and very stable conditions. *Bulletin of the American Meteorological Society*, 102, E218–E243.

Kral, S.T., Reuder, J., Vihma, T., Suomi, I., O'Connor, E., Kouznetsov, R., Wrenger, B., Rautenberg, A., Urbancic, G., Jonassen, M.O., Ba·serud, L., Maronga, B., Mayer, S., Lorenz, T., Holtslag, A.A.M., Steeneveld, G.-J., Seidl, A., Müller, M., Lindenberg, C., Langohr, C., Voss, H., Bange, J., Hundhausen, M., Hilsheimer, P. and Schygulla, M. (2018) Innovative strategies for observations in the Arctic atmospheric boundary layer (ISOBAR)—The Hailuoto 2017 campaign. *Atmosphere*, 9, 268.

Launiainen, J. and Cheng, B. (1998) Modelling of ice thermodynamics in natural water bodies. *Cold Regions Science and Technology*, 27, 153–178.

Mahrt, L. (2014) Stably stratified atmospheric boundary layers. *Annual Review of Fluid Mechanics*, 46, 23–45.

Mahrt, L. (2019) Microfronts in the nocturnal boundary layer. *Quarterly Journal of the Royal Meteorological Society*, 145, 546–562.

Mäkiranta, E., Vihma, T., Sjöblom, A. and Tastula, E.-M. (2011) Observations and modelling of the atmospheric boundary layer over sea-ice in a Svalbard fjord. *Boundary-Layer Meteorology*, 140, 105–123.

Mayer, S., Jonassen, M.O., Sandvik, A. and Reuder, J. (2012) Profiling the Arctic stable boundary layer in Advent Valley, Svalbard: Measurements and simulations. *Boundary-Layer Meteorology*, 143, 507–526.

Monin, A. and Obukhov, A. (1954) Basic laws of turbulent mixing in the surface layer of the atmosphere. *Contributions to the Geophysical Institute of the Academy of Sciences of the USSR*, 151, e187.

Nakanishi, M. and Niino, H. (2006) An improved Mellor–Yamada level-3 model: Its numerical stability and application to a regional prediction of advection fog. *Boundary-Layer Meteorology*, 119, 397–407.

Powers, J.G., Klemp, J.B., Skamarock, W.C., Davis, C.A., Dudhia, J., Gill, D.O., Coen, J.L., Gochis, D.J., Ahmadov, R., Peckham, S.E., Grell, G.A., Michalakes, J., Trahan, S., Benjamin, S.G., Alexander, C.R., Dimego, G.J., Wang, W., Schwartz, C.S., Romine, G.S., Liu, Z., Snyder, C., Chen, F., Barlage, M.J., Yu, W. and Duda, M.G. (2017) The Weather Research and Forecasting model: Overview, system efforts, and future directions. *Bulletin of the American Meteorological Society*, 98, 1717–1737.

Reuder, J., Jonassen, M.O. and Ólafsson, H. (2012) The Small Unmanned Meteorological Observer SUMO: Recent

developments and applications of a micro-UAS for atmospheric boundary layer research. *Acta Geophysica*, 60, 1454–1473.

Ronkainen, I., Lehtiranta, J., Lensu, M., Rinne, E., Haapala, J. and Haas, C. (2018) Interannual sea ice thickness variability in the Bay of Bothnia. *The Cryosphere*, 12, 3459–3476.

Savijärvi, H. and Kauhanen, J. (2001) High resolution numerical simulations of temporal and vertical variability in the stable wintertime boreal boundary layer: A case study. *Theoretical and Applied Climatology*, 70, 97–103.

Schneider, T., Lüpkes, C., Dorn, W., Chechin, D., Handorf, D., Khosravi, S., Gryanik, V.M., Makhotina, I. and Rinke, A. (2022) Sensitivity to changes in the surface-layer turbulence parameterization for stable conditions in winter: A case study with a regional climate model over the Arctic. *Atmospheric Science Letters*, 23, e1066.

Skamarock, W., Klemp, J., Dudhia, J., Gill, D., Barker, D., Duda, M., Huang, X., Wang, W. and Powers, J. (2008). A description of the Advanced Research WRF version 3 (NCAR Technical Note NCAR/TN-475+STR). Boulder, CO: National Center for Atmospheric Research. https://doi.org/10.5065/D68S4MVH.

Steeneveld, G.J., Van de Wiel, B.J.H. and Holtslag, A.A.M. (2006) Modeling the evolution of the atmospheric boundary layer coupled to the land surface for three contrasting nights in CASES-99. *Journal of the Atmospheric Sciences*, 63, 920–935.

Sterk, H.A.M., Steeneveld, G.J., Bosveld, F.C., Vihma, T., Anderson, P.S. and Holtslag, A.A.M. (2016) Clear-sky stable boundary layers with low winds over snow-covered surfaces. Part 2: Process sensitivity. *Quarterly Journal of the Royal Meteorological Society*, 142, 821–835.

Sterk, H.A.M., Steeneveld, G.J. and Holtslag, A.A.M. (2013) The role of snow-surface coupling, radiation, and turbulent mixing in modeling a stable boundary layer over Arctic sea ice. *Journal of Geophysical Research: Atmospheres*, 118, 1199–1217.

Sterk, H.A.M., Steeneveld, G.J., Vihma, T., Anderson, P.S., Bosveld, F.C. and Holtslag, A.A.M. (2015) Clear-sky stable boundary layers with low winds over snow-covered surfaces. Part 1: WRF model evaluation. *Quarterly Journal of the Royal Meteorological Society*, 141, 2165–2184.

Sukoriansky, S., Galperin, B. and Perov, V. (2005) Application of a new spectral theory of stably stratified turbulence to the atmospheric boundary layer over sea ice. *Boundary-Layer Meteorology*, 117, 231–257.

Tastula, E.-M., Galperin, B., Dudhia, J., LeMone, M.A., Sukoriansky, S. and Vihma, T. (2015) Methodical assessment of the differences between the QNSE and MYJ PBL schemes for stable conditions. *Quarterly Journal of the Royal Meteorological Society*, 141, 2077–2089.

Tewari, M., Chen, F., Wang, W., Dudhia, J., LeMone, M., Mitchell, K., Ek, M., Gayno, G., Wegiel, J. and Cuenca, R.H. (2004). Implementation and verification of the unified NOAH land surface model in the WRF model, American Meteorological Society, Seattle, WA.

Thompson, G., Field, P.R., Rasmussen, R.M. and Hall, W.D. (2008) Explicit forecasts of winter precipitation using an improved bulk microphysics scheme. Part II: Implementation of a new snow parameterization. *Monthly Weather Review*, 136, 5095–5115.

Tuomi, L., Kahma, K.K. and Pettersson, H. (2011) Wave hindcast statistics in the seasonally ice-covered Baltic Sea. *Boreal Environment Research*, 16, 451–472.

Uotila, P., Vihma, T. and Haapala, J. (2015) Atmospheric and oceanic conditions and the extremely low Bothnian Bay sea ice extent in 2014/2015. *Geophysical Research Letters*, 42, 7740–7749.

Walsh, J.E., Chapman, W.L., Romanovsky, V., Christensen, J.H. and Stendel, M. (2008) Global climate model performance over Alaska and Greenland. *Journal of Climate*, 21, 6156–6174.